Journal of
Materials Chemistry C

Accepted Manuscript

This article can be cited before page numbers have been issued, to do this please use: L. Huang, G. Han, B. Zhang and D. Gregory, *J. Mater. Chem. C*, 2019, DOI: 10.1039/C9TC01994D.

ROYAL SOCIETY OF CHEMISTRY

rsc.li/materials-c

View Article Online
DOI: 10.1039/C9TC01994D

Journal Name

ARTICLE

Anion-exchange Synthesis of Thermoelectric Layered $SnS_{0.1}Se_{0.9-x}Te_x$ Nano/microstructures in Aqueous Solution; Complexity and Carrier Concentration.†

Received 00th January 20xx,
Accepted 00th January 20xx

DOI: 10.1039/x0xx00000x

www.rsc.org/

Lisi Huang,[a] Guang Han,*[a,b] Bin Zhang,[c] and Duncan H. Gregory*[d]

Nanostructured $SnS_{0.1}Se_{0.9-x}Te_x$ (x = 0.02, 0.05, 0.08) quaternary chalcogenides have been controllably synthesised *via* a facile solution-processable anion-exchange method. All the products exist as "flower-like" architectures assembled from individual nano/microplates that are each hundreds of nanometers in thickness and several micrometers in lateral size. This morphology is essentially preserved from the original SnS starting material. Spark plasma sintering (SPS) not only consolidates the as-prepared powder samples, but also eliminates secondary phases, leading to pellets of phase-pure $SnS_{0.1}Se_{0.9-x}Te_x$ solid solution members. The electrical conductivity of $SnS_{0.1}Se_{0.88}Te_{0.02}$ is significantly enhanced over the Te-free material in the low-temperature range, achieving a peak value of ≈5760 S m^{-1} at 373 K, which is ≈41% higher than $SnS_{0.1}Se_{0.9}$ at the same temperature. Also possessing a high Seebeck coefficient, $SnS_{0.1}Se_{0.88}Te_{0.02}$ exhibits a maximum power factor (*ca.* 0.54 mW m^{-1} K^{-2}) at 423 K. The thermoelectric performance of $SnS_{0.1}Se_{0.9-x}Te_x$ has been optimised through modifying the Te concentration, leading to a peak *ZT* of ≈0.43 for $SnS_{0.1}Se_{0.88}Te_{0.02}$ at 773 K. This robust, scalable and surfactant-free approach paves the way to engineer increasingly complex (in this case, quaternary) metal chalcogenides controllably in aqueous solution.

Introduction

Renewable energy technologies play a vital part in addressing the over-consumption of fossil fuels and ever-increasing global energy demands.[1-5] Thermoelectrics, which enable direct and reversible conversion between thermal energy and electricity are perceived as potentially transformational in power generation and refrigeration. The energy conversion efficiency of a thermoelectric material is evaluated by its dimensionless figure of merit, $ZT = S^2\sigma T/\kappa$, where *S* is the Seebeck coefficient, σ the electrical conductivity, $S^2\sigma$ the power factor, κ the thermal conductivity and *T* the absolute temperature.[6-9] An excellent thermoelectric material should possess large Seebeck coefficient, high electrical conductivity and low thermal conductivity. Unfortunately, these parameters are correlated and extremely difficult to decouple, thus leading to palpable limits in *ZT*. To date, intensive efforts have been made to improve *ZT* through enhancement of the power factor ($S^2\sigma$) via energy filtering,[10, 11] electronic band convergence[12] and carrier concentration optimisation.[13-17] Alternatively attempts have been made to reduce thermal conductivity by nanostructuring[18-21] and by incorporation of nanoscale inclusions/precipitates[22-25] that introduce high-density interfaces, acting as phonon scattering centres.

Among emerging thermoelectric materials, lead-free binary tin chalcogenides (i.e., SnS, SnSe and SnTe) have proved to be promising candidates which also have the benefit of containing Earth-abundant and eco-friendly elements.[26-35] Recently, single crystalline SnSe has yielded record high *ZT* values of 2.6 and 2.3 at 923 K along the *b*- and *c*-axis, respectively, benefitting from the low values of κ that can be ascribed to anharmonic bonding.[26] In fact, the thermal transport properties of SnSe are subtle and complex and may also depend on the defect and surface chemistry of the single crystals.[4, 36, 37]Although some aspects of the thermal conducting behaviour of single-crystalline SnSe continue to benefit from further investigation,[38] the material undeniably forms the basis of systems for high-efficiency thermoelectric applications. [4, 32, 35] Hole doping can lead to multiple contributions to the valence band. The improved electrical conductivity and significantly enhanced values for the Seebeck coefficient can afford an exceptional device *ZT* of 1.34 (300 - 773 K).[30] Combining band engineering and point defect phonon scattering approaches generates ultra-high power factors and much-reduced thermal conductivity in single crystals with a composition of $Sn_{0.97}Na_{0.03}Se_{0.9}S_{0.1}$; an extraordinary average *ZT* of ≈1.6 can be achieved between 300 - 923 K.[39] However, applications of single crystals based on SnSe could be restricted by relatively poor mechanical properties. Polycrystalline materials could overcome such restrictions but unfortunately offer inferior *ZT* values, primarily originating from lesser electrical performance.[40] Various strategies to improve

[a] College of Materials Science and Engineering, Chongqing University, Chongqing 400044, China; *Email: guang.han@cqu.edu.cn
[b] Key Laboratory of Low-grade Energy Utilization Technologies and Systems, Ministry of Education, Chongqing University, Chongqing 400044, China
[c] Analytical and Testing Centre, Chongqing University, Chongqing 401331, China
[d] WestCHEM, School of Chemistry, University of Glasgow, Glasgow, G12 8QQ, UK; *Email: Duncan.Gregory@glasgow.ac.uk
† Electronic Supplementary Information (ESI) available. See
DOI: 10.1039/x0xx00000x

View Article Online
DOI: 10.1039/C9TC01094D

electrical conductivity and/or reduce lattice thermal conductivity have been successfully employed, such as doping (e.g. alkali metals,[41-44] Ag,[17, 45] Cu,[46] Bi[13]), forming solid solutions,[47, 48] and introducing precipitated phases.[23] However, the associated high-temperature syntheses of polycrystalline SnSe are energy-intensive and time-consuming. In contrast, if they can be successfully implemented, bottom-up wet-chemical methods would permit precise control over size, shape, structure and composition and additionally bring benefits of energy-efficiency and reduction of cost.[8, 49] For example, colloidal methods can efficiently produce nanocrystals with small size, tuneable morphology and uniform dispersion,[50] although such nanocrystals are often coated with residual insulating organic species, resulting in poor electrical conductivity.[51] Accordingly, organic-free solution routes can engineer products with impurity-free surfaces, achieving excellent electrical transport properties.[52, 53]

Metal chalcogenide quaternary systems have demonstrated excellent combinations of electrical and thermal properties. To date, there are limited reports on quaternary thermoelectric chalcogenide systems (e.g. $Bi_2Te_{2.7-x}Se_{0.3}S_x$,[54] $Cu_{2-y}S_{1/3}Se_{1/3}Te_{1/3}$[55] and PbTe-PbSe-PbS[56, 57]) and these compounds have been commonly prepared by high-temperature methods. In contrast, synthesising quaternary compounds in solution can be rather challenging and a level of difficulty greater than synthesising binary and ternary chalcogenides. To the best of our knowledge, there are no reports on the synthesis and thermoelectric performance of tin chalcogenides in the pseudo-quaternary Sn-S-Se-Te system. In this study, building on the success of synthesising ternary Sn-S-Se compounds in solution,[58] we have successfully synthesised a series of compositionally-modulated quaternary $SnS_{0.1}Se_{0.9-x}Te_x$ (x = 0.02, 0.05, 0.08) compounds *via* anion-exchange in aqueous solution using SnS nano/micro-plates as templates. Previous investigations indicate that substitution of Te in $SnSe_{1-x}Te_x$ not only produces more Sn vacancies, leading to enhanced carrier concentration, but also diminishes lattice thermal conductivity significantly with increasing Te substitution level when x < 0.1.[59] Therefore, we considered that if Te could be successfully substituted in $SnS_{0.1}Se_{0.9}$ (where the original Hall carrier concentration is of the order of 10^{18} cm^{-3} and lower than the optimal carrier concentration in SnSe)[58] then its electrical performance could be enhanced, and its lattice thermal conductivity might be further reduced. In fact, our studies show that the synthesised quaternary tin chalcogenide nano/microstructures can be consolidated into textured pellets with enhanced electrical conductivity and power factors over the low-temperature range when compared to Te-free $SnS_{0.1}Se_{0.9}$.

Experimental

Materials Synthesis. NaOH (Aladdin, 97%), $SnCl_2{\cdot}2H_2O$ (Aladdin, 99.99%), $Na_2S{\cdot}9H_2O$ (Aladdin, 99.99%), Te powder (Aladdin, 99.99%) and $NaBH_4$ (Alfa, 98%) were used without further purification. The first step in the synthesis leads to the formation of SnS nano/micro-plates. 50 ml of Na_2SnO_2 aqueous solution was prepared at room temperature (according to our previous report)[58] and heated to its boiling temperature using an oil bath. 40 ml of $Na_2S_{(aq)}$ (0.5 mol L^{-1}) was injected into the Na_2SnO_2 solution that was further boiled for 2 h, producing SnS plates. For the synthesis of $SnS_{0.1}Se_{0.9-x}Te_x$ (x = 0.02, 0.05, 0.08), 5 ml of freshly prepared $NaHTe_{(aq)}$ (0.04, 0.1, 0.16 mol L^{-1}) (the preparation procedure of $NaHTe_{(aq)}$ can be found in a previous report[53]) was promptly injected into the SnS suspension that was boiled for a further 1.5 h. 40 ml of freshly prepared $NaHSe_{(aq)}$ (0.25 mol L^{-1}) was subsequently swiftly injected into the above suspension, which was boiled for 2 h before cooling to room temperature. Heating and cooling of the solution were performed under the protection of Ar gas (Wangmiao, 99.999%). The products were cleaned with deionised water and ethanol and dried under vacuum at 60 ºC for 12 h. The synthesised samples were loaded in glass vessels and stored in an Ar-filled DELLIX glovebox (< 0.1 ppm H_2O, < 0.1 ppm O_2) to avoid oxidation. Scaled-up syntheses of $SnS_{0.1}Se_{0.9-x}Te_x$ were performed with 3.5-fold increases in the amount of the precursors. $SnS_{0.1}Se_{0.9-x}Te_x$ powders were spark plasma sintered (SPS) at 500 °C for 5 min into dense pellets under vacuum and a uniaxial pressure of 60 MPa. The SPS process resulted in a series of $SnS_{0.1}Se_{0.9-x}Te_x$ cylinders with densities of *ca.* 6.06 - 6.09 g cm^{-3}.

Materials Characterisation. Powder X-ray diffraction (XRD) analysis of the powder samples was performed using PANalytical X'pert and Rigaku D/max 2500PC diffractometers (both with Cu Kα radiation). Rietveld refinement against XRD data was performed using the GSAS and EXPGUI software packages.[60, 61] The degree of crystal plane orientation was also estimated by the Lotgering method[62] in order to evaluate the extent of texturing in the pellets directly. The orientation degree (F) of the (h00) planes was calculated by $F = (P-P_0)/(1-P_0)$, where $P_0 = I_0(h00)/\Sigma I_0(hkl)$, $P = I(h00)/\Sigma I(hkl)$ and I_0 and I are the integrated peak intensities of a randomly orientated sample and the measured sample, respectively. Scanning electron microscopy (JEOL JSM-7800F microscope) and associated energy dispersive X-ray spectroscopy (EDS) (80 mm^2 X-Max, Oxford Instruments) experiments were performed for imaging (5 kV incident beam) and elemental analysis (20 kV incident beam) respectively. Transmission electron microscopy (TEM, FEI Talos F200S G2 equipped with Super-X windowless EDS detector, operated at 200 kV) experiments were performed for further imaging, elemental analysis and selected area electron diffraction (SAED).

Performance Evaluation. The electrical and thermal properties were both measured on pellets perpendicular to the pressing direction. Both electrical conductivity (σ) and Seebeck coefficient (S) of the pellets were measured using a Linseis LSR-3 instrument from 323 - 773 K. The total thermal conductivity (κ_{total}) was calculated from the expression $\kappa_{total} = DC_p\rho$ (where D, C_p and ρ are the thermal diffusivity, specific heat capacity and density, respectively). The thermal diffusivity, D for the $SnS_{0.1}Se_{0.9-x}Te_X$ pellets was measured using a Netzsch LFA 457 instrument from 323 - 773 K; the specific heat capacity, C_p of $SnS_{0.1}Se_{0.9-x}Te_x$ was calculated from the weighted average of the reported C_p values of SnS,[27] SnSe[26] and SnTe[33]; the density, ρ of

$SnS_{0.1}Se_{0.9-x}Te_x$ was measured by the Archimedes method. The electronic thermal conductivity (κ_e) was estimated from the Wiedemann-Franz law ($\kappa_e = L\sigma T$, where L is the Lorentz number, and a value of $L = 1.5 \times 10^{-8}$ V^2 K^{-2} was used in this study[26]). The lattice thermal conductivity (κ_L) was obtained by subtracting κ_e from κ_{total}. The figure of merit, ZT, was calculated according to $ZT = S^2\sigma T/\kappa$. Hall measurements were performed under an applied magnetic field of ±1 T using a Hall apparatus built in-house.

Results and discussion

We employed a stepwise anion-exchange method to engineer quaternary $SnS_{0.1}Se_{0.9-x}Te_x$ compounds (x = 0.02, 0.05, 0.08) by successively injecting appropriate amounts of NaHTe and NaHSe aqueous solutions into a SnS suspension and boiling for *ca*. 1.5 - 2 h after each mixing process. The anion exchange is enabled by the discrepant solubility of different tin chalcogenides (i.e., K_{sp}(SnS) > K_{sp}(SnSe) > K_{sp}(SnTe); K_{sp} is the solubility product).[63] Figure 1a shows the XRD patterns from samples of as-synthesised $SnS_{0.1}Se_{0.9-x}Te_x$ (x = 0.02, 0.05, 0.08). The majority of the diffraction peaks for all the samples can be indexed to an SnSe-type phase in orthorhombic space group *Pnma* (JCPDS No. 48-1224). An almost negligible amount of SnS (JCPDS No. 73-1859) phase (denoted as open red diamonds in Figure 1a) is observed in all the powder samples, which is consistent with our previous study.[58] When x reaches a value of 0.08, reflections corresponding to SnTe (JCPDS No. 46-1210; labelled by blue triangles in Figure 1a) become evident in the diffraction patterns. Figure 1b provides a magnified view of the region of the diffraction patterns containing the (111) and (400) Bragg peaks from the SnSe-type phase. Both peaks apparently shift to lower angles with increasing Te concentration as compared to those of $SnS_{0.1}Se_{0.9}$. This is consistent with the larger ionic radius of Te^{2-} (2.07 Å) over Se^{2-} (1.84 Å)[64] and an expansion of the orthorhombic unit cell as Te replaces Se.

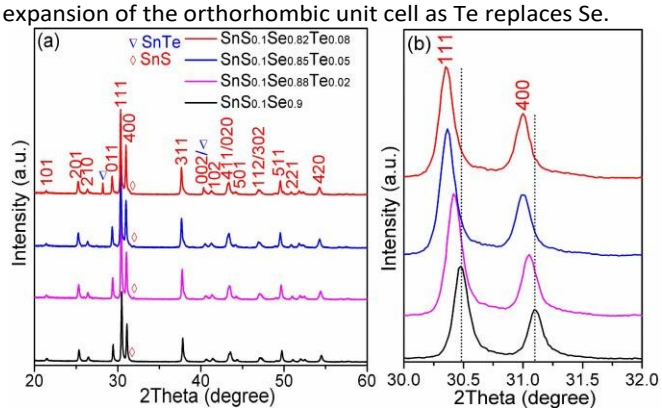

Figure 1. (a) XRD patterns for $SnS_{0.1}Se_{0.9-x}Te_x$ samples with x = 0.02, 0.05, 0.08 as compared to that of $SnS_{0.1}Se_{0.9}$; (b) enlarged (111) and (400) diffraction peaks in the range $30 \le 2\theta/^\circ \le 32$. The dashed lines indicate the (111) and (400) Bragg reflections of $SnS_{0.1}Se_{0.9}$. The (hkl) indices correspond to the SnSe phase.

The low- and high-magnification SEM images for all the samples are displayed in Figure 2a-f. SEM images indicate that all the products are assembled as "flower-like" nano/microstructures, composed of a number of nano/micro-plates, which are very similar to the morphology we previously observed for $SnS_{0.1}Se_{0.9}$ and SnS prepared by similar methods.[58] For x = 0.02, it can be seen that these architectures consist of plates with thicknesses of *ca*. 100 nm - 2 µm and lateral dimensions of *ca*. 1.5 - 7 µm. As the Te concentration increases the morphology of the samples begins to change such that by x = 0.08 the plates become more fragmented and typically measure *ca*. 0.4 - 6 µm across. EDS spectra (typical ones are shown in Figure 2g-i) confirm that the average chemical formulae can be approximated as $SnS_{0.11}Se_{0.88}Te_{0.01}$, $SnS_{0.10}Se_{0.86}Te_{0.04}$ and $SnS_{0.09}Se_{0.84}Te_{0.07}$ (with estimated errors of approximately 6% for each element) for the samples with x = 0.02, 0.05 and 0.08, respectively, which are close to the intended (nominal) compositions for the quaternary chalcogenides.

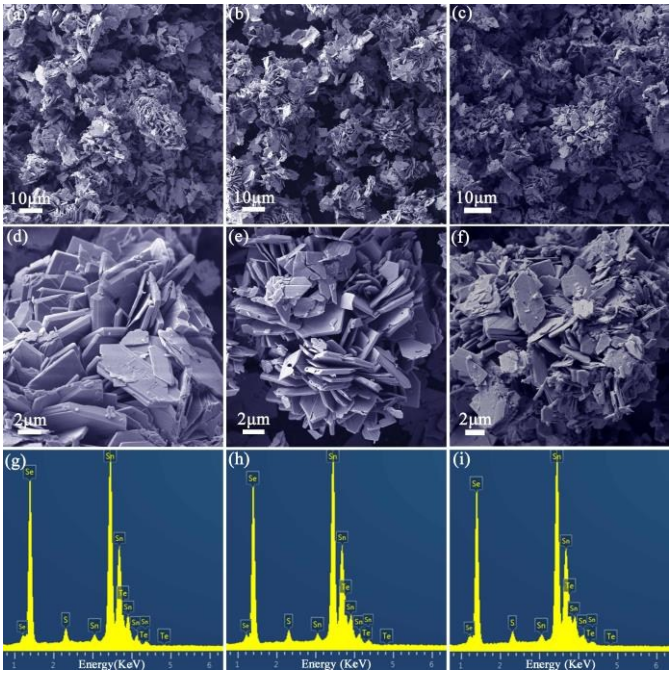

Figure 2. (a-c) Low-magnification SEM images, (d-f) high-magnification SEM images and (g-i) EDS spectra for $SnS_{0.1}Se_{0.9-x}Te_x$ samples with x = 0.02, 0.05, 0.08, respectively (See also ESI, Figure S1 for further information).

Figure 3a shows a TEM image of an isolated plate of $SnS_{0.1}Se_{0.88}Te_{0.02}$. Its SAED pattern along the [100] zone axis is displayed in Figure 3b, indicating the single crystallinity of the plate. A high-resolution transmission electron microscopy (HRTEM) image of the plate (Figure 3c) demonstrates a series of *d*-spacings of 2.9 Å with an intersection angle of 93° which correspond to the {011} planes of $SnS_{0.1}Se_{0.88}Te_{0.02}$. From a comparison with our previous work on $SnS_{0.1}Se_{0.9}$,[58] it is evident that the crystal structure is effectively unaltered during the anion-exchange process. Figure 3d depicts the high angle annular dark field-scanning transmission electron microscopy (HAADF-STEM) image and corresponding elemental mapping results from $SnS_{0.1}Se_{0.88}Te_{0.02}$, indicating slight enrichment of S in the centre of plate. Our previous investigations demonstrate that SnS plates can access Se^{2-} from both the faces and edges, which results in nanoplates that are richer in S at the plate centre.[58] An analogous process with Te^{2-} and Se^{2-} occurs in this present study. EDS element maps were also collected from the $SnS_{0.1}Se_{0.82}Te_{0.08}$ sample to verify the nature of the nanoparticles formed. These show that when the added concentration of Te^{2-} is at its highest, then there are two types

of nanoparticles present in addition to the majority $SnS_{0.1}Se_{0.82}Te_{0.08}$ nanosheets; these are either SnTe@Se core-shell structures (Figure S2) or nanoparticles of elemental Se (Figure S3). As NaHSe solution was injected, it can be deduced that the excess NaHSe was partially oxidised and coated the SnTe particles that had already crystallised from solution. Further work is being performed to understand the exact mechanism of this process such that Se can be coated on the SnTe particles controllably to synthesise core-shell particles of predetermined dimensions. It is interesting to note that no diffraction peak of Se is observed in the XRD pattern of $SnS_{0.1}Se_{0.82}Te_{0.08}$ sample, indicating that the Se that is formed and observed by TEM is amorphous and/or is present at very low levels.

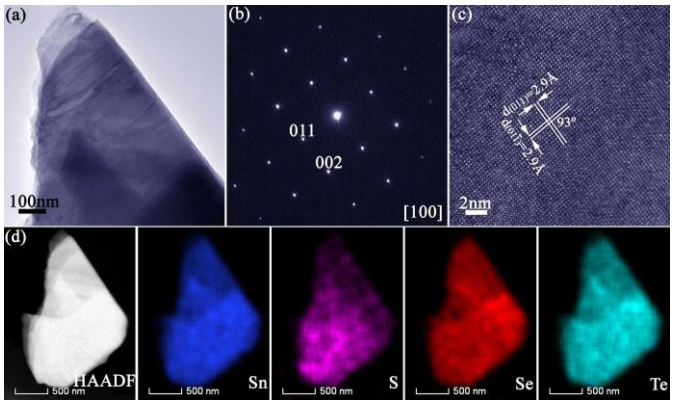

Figure 3. (a) TEM image of a $SnS_{0.1}Se_{0.88}Te_{0.02}$ plate; (b) its corresponding SAED pattern along the [100] zone axis; (c) HRTEM image; (d) HAADF-STEM image and corresponding element maps for Sn, S, Se, Te, respectively.

The scaled-up variant of the synthesis can yield more than 6 g of quaternary chalcogenide powders, which were prepared as dense pellets *via* spark plasma sintering (SPS) for performance evaluation. In view of the anisotropy of the crystal structure, XRD patterns for the SPS-treated $SnS_{0.1}Se_{0.9-x}Te_x$ pellets with x = 0.02, 0.05 and 0.08 (denoted "SPS-$SnS_{0.1}Se_{0.9-x}Te_x$") were collected parallel and perpendicular to the pressing direction, respectively, as shown in Figure 4. It is clear that all the diffraction peaks can be exclusively indexed to the *Pnma* structure of SnSe (JCPDS No. 48-1224) with no indication of any impurity peaks (e.g. SnS, SnTe, Se) for any of the pellets. The intensities of the (400) diffraction peak in all of the XRD patterns collected perpendicular to the pressing direction (Figure 4b) are significantly enhanced, indicating strong preferred orientation in the pellets. The degree of texturing for the pellets, which is intimately related to the orientation degree (*F*) of the (400) plane, was estimated from the XRD patterns (Figure 4b) by applying the Lotgering method.[62] The calculated value of *F* is 0.46, 0.41 and 0.37 for the x = 0.02, 0.05 and 0.08 pellets, respectively. Each of the lattice parameters, *a*, *b* and *c* (and therefore the unit cell volumes) of the $SnS_{0.1}Se_{0.9-x}Te_x$ pellets increase almost linearly with increasing Te concentration (x), broadly following Vegard's Law as might be expected as larger Te^{2-} replaces Se^{2-}(Figure S4).

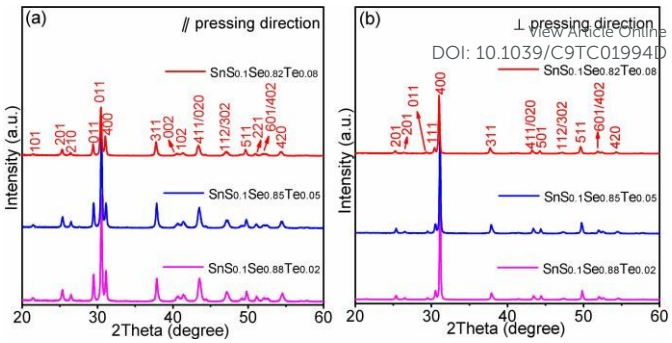

Figure 4. XRD patterns for SPS-$SnS_{0.1}Se_{0.9-x}Te_x$ pellets with x = 0.02, 0.05, 0.08 measured (a) parallel and (b) perpendicular to the pressing direction, respectively.

Figure 5a-c and 5d-f depict SEM images for SPS-$SnS_{0.1}Se_{0.9-x}Te_x$ samples (x = 0.02, 0.05, 0.08) along the perpendicular and parallel directions respectively to pressing. The microstructures, consisting of microplates, are dense for all the samples. Additionally, a large percentage of plates show a nearly parallel arrangement to the pellet surface (Figure 5d-f), which coincides with the anisotropy in the microstructure demonstrated by XRD results. Typical EDS spectra for all the SPS samples are shown in Figure 5g-i. The average chemical formulae are approximately $SnS_{0.11}Se_{0.87}Te_{0.02}$, $SnS_{0.11}Se_{0.85}Te_{0.04}$ and $SnS_{0.11}Se_{0.82}Te_{0.07}$ for the pellets with x = 0.02, 0.05 and 0.08, respectively, indicating that the atomic ratios are essentially unchanged after the SPS process. Moreover, in some contrast to the heterogeneity in the element distribution seen in the pre-sintered nanoplates (Figure 3d, S2), each of the constituent elements (and notably the chalcogens) are more uniformly distributed in SPS-$SnS_{0.1}Se_{0.88}Te_{0.02}$ (Figures 6, S6) and SPS-$SnS_{0.1}Se_{0.82}Te_{0.08}$ (Figure S7, S8). This observation would lend weight to the premise that the elevated temperature and pressure of the SPS process promotes the re-distribution of chalcogens and facilitates the formation of each of the quaternary solid solution members across the entire volume of each of the pellets.

View Article Online
DOI: 10.1039/C9TC01994D

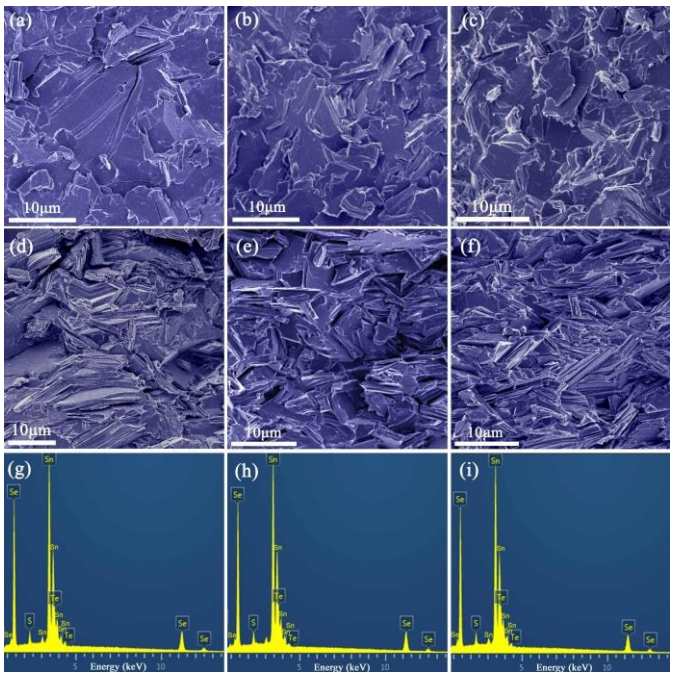

Figure 5. Cross-sectional SEM images taken from fractured pellets along directions (a-c) perpendicular and (d-f) parallel to pressing and (g-i) EDS spectra for SPS-$SnS_{0.1}Se_{0.9-x}Te_x$ samples with x = 0.02, 0.05, 0.08, respectively (collected from sections perpendicular to pressing; the SEM images revealing the positions from which EDS spectra were collected are given in Figure S5).

Electrical and thermal transport measurements were taken perpendicular to the pressing direction, as shown in Figure 7. The thermoelectric performance of a $SnS_{0.1}Se_{0.9}$ pellet[58] with a very similar degree of texturing (preferred orientation of the (400) plane) to the $SnS_{0.1}Se_{0.9-x}Te_x$ samples is also included for comparison in order to understand the influence of replacing Se by Te on the thermoelectric performance (while simultaneously excluding the influence of texturing).[65-67] Figure 7a presents plots of the electrical conductivity (σ) as a function of temperature for all the samples. For SPS-$SnS_{0.1}Se_{0.9-x}Te_x$ (x = 0.02, 0.05) samples, initially (below 450 K), σ increases with increasing temperature, conforming to the expected semiconducting behaviour. Subsequently the conductivity decreases until approximately 673 K, which is more indicative of metallic behaviour. Finally σ begins to increase again (until the maximum measurement temperature) which could be attributed to the thermal activation of minority carriers.[68] For x = 0.08, however, the behaviour is very different, with σ first declining up to 623 K then increasing at higher temperatures. Interestingly, at 323 K, all the SPS-$SnS_{0.1}Se_{0.9-x}Te_x$ samples possess a higher electrical conductivity than $SnS_{0.1}Se_{0.9}$ ($\sigma_{323\ K} \approx$ 3030 S m^{-1}, 5030 S m^{-1}, 3930 S m^{-1} and 4140 S m^{-1} for x = 0, 0.02, 0.05 and 0.08 samples, respectively). This behaviour might be rationalised in terms of the carrier concentration (n_H) which could increase with increasing Sn deficiency. One would also expect the Fermi level to move towards the valence band as Te substitutes for Se.[59] Indeed, from Hall measurements, the Te-substituted samples reveal enhanced values of n_H, as shown in Table 1. The electrical conductivity in the lower temperature regime peaks for $SnS_{0.1}Se_{0.88}Te_{0.02}$, achieve the highest value of σ at 373 K (*ca*. 5760 S m^{-1}), which is approximately 41% higher than the electrical conductivity of $SnS_{0.1}Se_{0.9}$ at the same temperature. It is interesting to note that the carrier mobility (μ_H) for Te-containing samples decreases compared to that for $SnS_{0.1}Se_{0.9}$, which could be related to additional carrier scattering effects in the Te-substituted samples. Reduced carrier mobility is also observed when Te is substituted for Se in $SnSe_{1-x}Te_x$[59] and further investigation will be required to clarify the origin of this scattering in Te-containing materials.

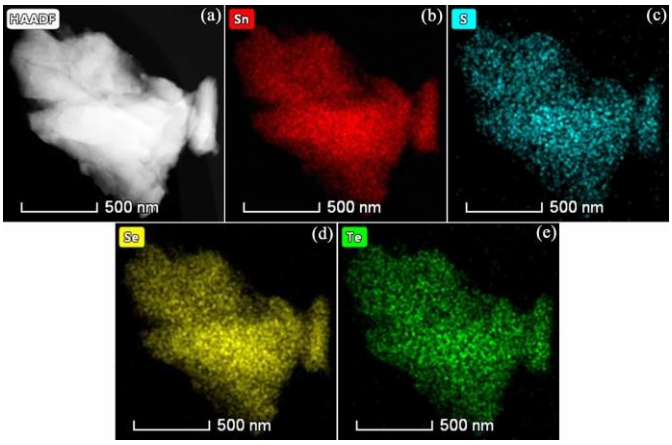

Figure 6. Characterisation of a SPS-$SnS_{0.1}Se_{0.88}Te_{0.02}$ pellet: (a) HAADF-STEM image and (b-e) corresponding element maps for Sn, S, Se and Te, respectively.

Figure 7b displays the temperature-dependent values of the Seebeck coefficient (*S*). For all the samples, positive values of *S* demonstrate p-type conductive behaviour. These values increase up to *ca*. 623-673 K and then subsequently decrease with further increasing temperature owing to the bipolar effect.[59] Compared with $SnS_{0.1}Se_{0.9}$, a larger Seebeck coefficient is obtained for the x = 0.05 sample over the entire temperature range, while, for x = 0.02 and 0.08, *S* is higher than the x = 0 materials above *ca*. 623 K and *ca*. 523 K, respectively. Notably, the maximum in *S* increases from approx. 400 μV K^{-1} for $SnS_{0.1}Se_{0.9}$ to approx. 430 μV K^{-1} for $SnS_{0.1}Se_{0.85}Te_{0.05}$. The corresponding temperature dependence of the power factors (*PFs*) for all the samples is shown in Figure 7c. For x = 0.02, the *PF* exceeds that of $SnS_{0.1}Se_{0.9}$ below 473 K, (peaking at *ca*. ≈0.54 mW m^{-1} K^{-2} at 423 K, while $Sn_{0.99}Na_{0.01}Se_{0.84}Te_{0.16}$ only achieves *PF* ≈ 0.33 mW m^{-1} K^{-2} at the same temperature).[69] Whereas the *PFs* for x = 0.05 and 0.08 surpass that of $SnS_{0.1}Se_{0.9}$ slightly above ambient temperature (< 370 K), the values do not compare favourably as the temperature increases further.

Considering the thermal properties, the total thermal conductivity (κ_{total}) is plotted as a function of temperature in Figure 7d. The corresponding lattice thermal conductivity (κ_L) is shown in Figure 7e and exhibits much the same temperature-dependence as κ_{total}. Increasing the Te concentration only marginally decreases the κ_L in the SPS-$SnS_{0.1}Se_{0.9-x}Te_x$ materials as compared to $SnS_{0.1}Se_{0.9}$. κ_L is related to Umklapp, grain boundary and defect scattering.[69, 70] Considering the similar grain sizes of all the samples, it is not perhaps surprising that grain boundary scattering effects should be very similar. Replacement of Se by Te introduces point defect scattering consistent with the different ionic radii of Se^{2-} and Te^{2-}.[70] However, previous reports have suggested that introduction of Te may moderate Umklapp scattering, resulting from a

weakening of the anharmonic bonding and a variation in the bonding instability in Te-substituted SnSe.[59] In light of these likely competing influences on the phonon scattering, Te replacement leads to only a slight reduction of κ_L. The lowest total thermal conductivity ($\kappa_{total} \approx 0.67$ W m^{-1} K^{-1}) exists for SPS-$SnS_{0.1}Se_{0.82}Te_{0.08}$ at 773 K. Previous investigations of the $SnSe_{1-x}Te_x$ system have suggested that at Te substitution levels below 10% ($x < 0.1$ in $SnSe_{1-x}Te_x$), κ_L decreases as more Te is substituted, whereas for $0.1 \leq x \leq 0.2$ the reduction in κ_L is insignificant. [59,69] In light of these previous reports, it is of interest to note that κ_{total} and κ_L for $SnS_{0.1}Se_{0.9-x}Te_x$ samples with (S+Te) atomic concentration of 12-18% are only marginally less between *ca.* 323-423 K than $SnS_{0.1}Se_{0.9}$ itself (Figure 7d,e).

The corresponding temperature variation in the figure of merit, *ZT* is displayed in Figure 7f. The *ZT* values for all the samples rise with increasing temperature. With the contribution of higher σ (and *PF*s), $SnS_{0.1}Se_{0.9-x}Te_x$ possess higher *ZT* values when compared to $SnS_{0.1}Se_{0.9}$, (*ZT* ≈ 0.09 for all $x > 0$ at 323 K, representing a ≈ 50% enhancement over $SnS_{0.1}Se_{0.9}$). At lower temperatures, it is thus possible to maximise the thermoelectric performance of $SnS_{0.1}Se_{0.9-x}Te_x$ by substituting a small amount (≈ 2%) of Te for Se (giving *ZT* ≈ 0.43 at 773 K for $x = 0.02$). Considering that the solubility product, K_{sp}, values of metal chalcogenides generally increase with decreasing chalcogenide anionic radius ($K_{sp}(M_xTe_y) < K_{sp}(M_xSe_y) < K_{sp}(M_xS_y)$; M denotes a given metal),[63] the anion-exchange approach demonstrated in this study could be extended to the synthesis of other quaternary metal chalcogenides (including Cu- and Pb-based systems, for example) in order to tune their electrical and thermal properties and therefore enhance their thermoelectric performance.

Table 1. Hall carrier concentration (n_H) and carrier mobility (μ_H) at room temperature of the SPS-$SnS_{0.1}Se_{0.9-x}Te_x$ ($x = 0.02, 0.05, 0.08$) pellets.

Pellets	n_H [10^{18} cm^{-3}]	μ_H [cm^2 V^{-1} s^{-1}]	References
$SnS_{0.1}Se_{0.9}$	2.6	65.0	[58]
$SnS_{0.1}Se_{0.88}Te_{0.02}$	11.1	26.7	This work
$SnS_{0.1}Se_{0.85}Te_{0.05}$	8.5	29.1	This work
$SnS_{0.1}Se_{0.82}Te_{0.08}$	10.3	25.5	This work

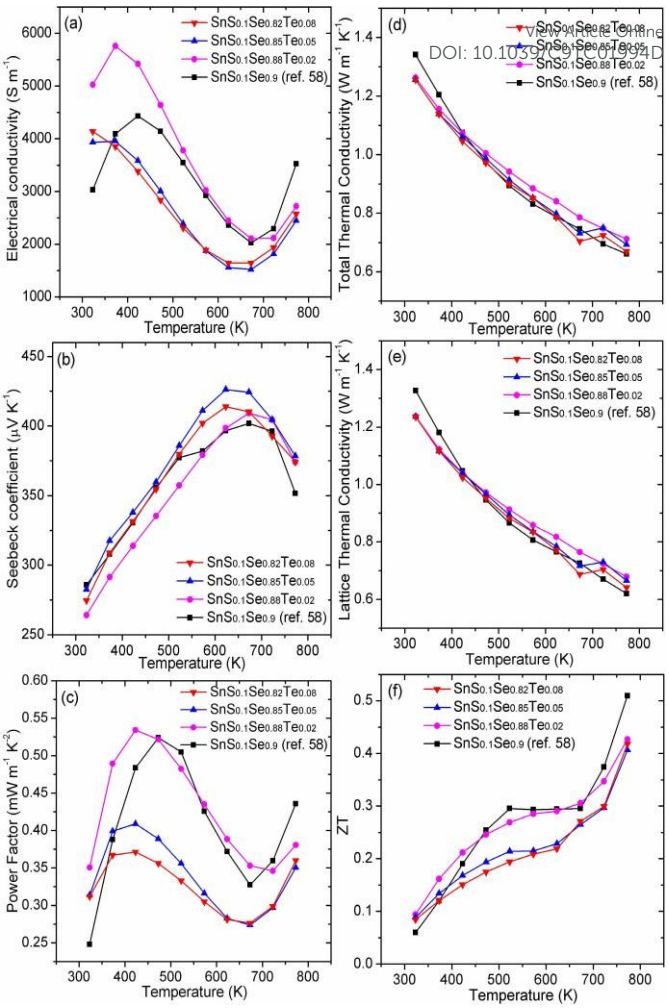

Figure 7. Temperature dependence of (a) electrical conductivity, (b) Seebeck coefficient, (c) power factor, (d) total thermal conductivity, (e) lattice thermal conductivity and (f) *ZT* for $SnS_{0.1}Se_{0.9-x}Te_x$ samples with $x = 0.02$ (red triangles), 0.05 (blue triangles), 0.08 (magenta circles) measured perpendicular to the pressing direction. Data for the Te-containing samples are compared with those for $SnS_{0.1}Se_{0.9}$ from ref. 58.

Conclusions

In summary, we employed a facile and versatile, organic-free anion-exchange method in the synthesis of layered $SnS_{0.1}Se_{0.9-x}Te_x$ quaternary chalcogenides with modulated Te compositions of $x = 0.02$, 0.05 and 0.08. All the samples reveal a "flower-like" morphology in which the micron-sized flowers are constructed from the intricate arrangement of individual nano/micro-plates. Increased carrier concentration is responsible for the remarkable improvement in the electrical conductivity of the p-type Te-substituted chalcogenides in the low-temperature regime. The highest electrical conductivity of *ca.* 5760 S m^{-1} at 373 K and the maximum power factor of *ca.* 0.54 mW m^{-1} K^{-2} at 423 K are achieved for the $x = 0.02$ sample. Tuning the Te concentration proves to be a very effective route to optimise the thermoelectric performance of quaternary chalcogenides. and a maximum value of *ZT* can be achieved by introducing 2% of Te into $SnS_{0.1}Se_{0.9}$ (*ZT* ≈ 0.43 at 773 K for $SnS_{0.1}Se_{0.88}Te_{0.02}$). The success of this strategy suggests a broader opportunity to synthesise complex multinary chalcogenide thermoelectrics with precise compositional and microstructural control.

Moreover, such materials can be produced in aqueous solution *via* a simple scalable, organic-free process.

Conflicts of interest

There are no conflicts to declare.

Acknowledgements

This work was financially supported by the National Natural Science Foundation of China (No. 51802034), the Chongqing Research Program of Basic Research and Frontier Technology (No. cstc2018jcyjAX0346), the Chongqing Entrepreneurship and Innovation Program for the Returned Overseas Chinese Scholars (No. cx2018020), the Fundamental Research Funds for the Central Universities (No. 2019CDQYCL003), and the Research Funds from Key Laboratory of Low-grade Energy Utilization Technologies and Systems, Ministry of Education, Chongqing University (LLEUTS-201802). We would like to acknowledge Analytical and Testing Centre of Chongqing University for accessing characterisation and performance measurement facilities.

References

1. L.-D. Zhao, V. P. Dravid and M. G. Kanatzidis, *Energy Environ. Sci.*, 2014, **7**, 251-268.
2. A. J. Minnich, M. S. Dresselhaus, Z. F. Ren and G. Chen, *Energy Environ. Sci.*, 2009, **2**, 466-479.
3. G. Han, Z.-G. Chen, J. Drennan and J. Zou, *Small*, 2014, **10**, 2747-2765.
4. L.-D. Zhao, C. Chang, G. Tan and M. G. Kanatzidis, *Energy Environ. Sci.*, 2016, **9**, 3044-3060.
5. R. Nunna, P. Qiu, M. Yin, H. Chen, R. Hanus, Q. Song, T. Zhang, M.-Y. Chou, M. T. Agne, J. He, G. J. Snyder, X. Shi and L. Chen, *Energy Environ. Sci.*, 2017, **10**, 1928-1935.
6. L. E. Bell, *Science*, 2008, **321**, 1457-1461.
7. G. Tan, L. D. Zhao and M. G. Kanatzidis, *Chem. Rev.*, 2016, **116**, 12123-12149.
8. S. Ortega, M. Ibanez, Y. Liu, Y. Zhang, M. V. Kovalenko, D. Cadavid and A. Cabot, *Chem. Soc. Rev.*, 2017, **46**, 3510-3528.
9. Y. Zheng, Y. Luo, C. Du, B. Zhu, Q. Liang, H. H. Hng, K. Hippalgaonkar, J. Xu and Q. Yan, *Mater. Chem. Front.*, 2017, **1**, 2457-2473.
10. Y. Min, J. W. Roh, H. Yang, M. Park, S. I. Kim, S. Hwang, S. M. Lee, K. H. Lee and U. Jeong, *Adv. Mater.*, 2013, **25**, 1425-1429.
11. J.-H. Bahk, Z. Bian and A. Shakouri, *Phys. Rev. B*, 2013, **87**, 075204.
12. Y. Pei, X. Shi, A. LaLonde, H. Wang, L. Chen and G. J. Snyder, *Nature*, 2011, **473**, 66-69.
13. A. T. Duong, V. Q. Nguyen, G. Duvjir, V. T. Duong, S. Kwon, J. Y. Song, J. K. Lee, J. E. Lee, S. Park, T. Min, J. Lee, J. Kim and S. Cho, *Nat. Commun.*, 2016, **7**, 13713.
14. Y. Luo, Y. Zheng, Z. Luo, S. Hao, C. Du, Q. Liang, Z. Li, K. A. Khor, K. Hippalgaonkar, J. Xu, Q. Yan, C. Wolverton and M. G. Kanatzidis, *Adv. Energy Mater.*, 2018, **8**, 1702167.
15. X. Wang, J. Xu, G. Liu, Y. Fu, Z. Liu, X. Tan, H. Shao, H. Jiang, T. Tan and J. Jiang, *Appl. Phys. Lett.*, 2016, **108**, 083902.
16. Q. Zhang, E. K. Chere, J. Sun, F. Cao, K. Dahal, S. Chen, G. Chen and Z. Ren, *Adv.Energy Mater.*, 2015, **5**, 1500360.
17. C.-L. Chen, H. Wang, Y.-Y. Chen, T. Day and G. J. Snyder, *J. Mater. Chem. A*, 2014, **2**, 11171-11176.
18. A. Zhang, B. Zhang, W. Lu, D. Xie, H. Ou, X. Han, J. Dai, X. Lu, G. Han, G. Wang and X. Zhou, *Adv. Funct. Mater.*, 2018, **28**, 1705117.
19. G. Han, Z. G. Chen, L. Yang, M. Hong, J. Drennan and J. Zou, *ACS Appl. Mater. Interfaces*, 2015, **7**, 989-995.
20. F. J. Fan, Y. X. Wang, X. J. Liu, L. Wu and S. H. Yu, *Adv. Mater.*, 2012, **24**, 6158-6163.
21. S. N. Girard, J. He, X. Zhou, D. Shoemaker, C. M. Jaworski, C. Uher, V. P. Dravid, J. P. Heremans and M. G. Kanatzidis, *J. Am. Chem. Soc.*, 2011, **133**, 16588-16597.
22. Y. Xiao, H. Wu, W. Li, M. Yin, Y. Pei, Y. Zhang, L. Fu, Y. Chen, S. J. Pennycook, L. Huang, J. He and L. D. Zhao, *J. Am. Chem. Soc.*, 2017, **139**, 18732-18738.
23. G. Tang, W. Wei, J. Zhang, Y. Li, X. Wang, G. Xu, C. Chang, Z. Wang, Y. Du and L. D. Zhao, *J. Am. Chem. Soc.*, 2016, **138**, 13647-13654.
24. Y.-X. Chen, Z.-H. Ge, M. Yin, D. Feng, X.-Q. Huang, W. Zhao and J. He, *Adv. Funct. Mater.*, 2016, **26**, 6836-6845.
25. S. N. Girard, T. C. Chasapis, J. He, X. Zhou, E. Hatzikraniotis, C. Uher, K. M. Paraskevopoulos, V. P. Dravid and M. G. Kanatzidis, *Energy Environ. Sci.*, 2012, **5**, 8716-8725.
26. L. D. Zhao, S. H. Lo, Y. Zhang, H. Sun, G. Tan, C. Uher, C. Wolverton, V. P. Dravid and M. G. Kanatzidis, *Nature*, 2014, **508**, 373-377.
27. Q. Tan, L. D. Zhao, J. F. Li, C. F. Wu, T. R. Wei, Z. B. Xing and M. G. Kanatzidis, *J. Mater. Chem. A*, 2014, **2**, 17302-17306.
28. R. Moshwan, L. Yang, J. Zou and Z. G. Chen, *Adv. Funct. Mater.*, 2017, **27**, 18.
29. X. L. Shi, A. Wu, T. L. Feng, K. Zheng, W. D. Liu, Q. Sun, M. Hong, S. T. Pantelides, Z. G. Chen and J. Zou, *Adv. Energy Mater.*, 2019, **9**, 1803242.
30. L. D. Zhao, G. Tan, S. Hao, J. He, Y. Pei, H. Chi, H. Wang, S. Gong, H. Xu, V. P. Dravid, C. Uher, G. J. Snyder, C. Wolverton and M. G. Kanatzidis, *Science*, 2016, 141-144.
31. J. Tang, B. Gao, S. Lin, X. Wang, X. Zhang, F. Xiong, W. Li, Y. Chen and Y. Pei, *ACS Energy Lett.*, 2018, **3**, 1969-1974.
32. Z.-G. Chen, X. Shi, L.-D. Zhao and J. Zou, *Prog. Mater Sci.*, 2018, **97**, 283-346.
33. Q. Zhang, B. L. Liao, Y. C. Lan, K. Lukas, W. S. Liu, K. Esfarjani, C. Opeil, D. Broido, G. Chen and Z. F. Ren, *Proc. Natl. Acad. Sci.*, 2013, **110**, 13261-13266.
34. X. L. Shi, K. Zheng, W. D. Liu, Y. Wang, Y. Z. Yang, Z. G. Chen and J. Zou, *Adv. Energy Mater.*, 2018, **8**, 1800775.
35. X. Zhou, Y. Yan, X. Lu, H. Zhu, X. Han, G. Chen and Z. Ren, *Mater. Today*, 2018, **21**, 974-988.
36. D. Wu, L. J. Wu, D. S. He, L. D. Zhao, W. Li, M. H. Wu, M. Jin, J. T. Xu, J. Jiang, L. Huang, Y. M. Zhu, M. G. Kanatzidis and J. Q. He, *Nano Energy*, 2017, **35**, 321-330.
37. Y. K. Lee, Z. Luo, S. P. Cho, M. G. Kanatzidis and I. Chung, *Joule*, 2019, **3**, 719-731.
38. P. C. Wei, S. Bhattacharya, J. He, S. Neeleshwar, R. Podila, Y. Y. Chen and A. M. Rao, *Nature*, 2016, **539**, E1-E2.
39. K. Peng, B. Zhang, H. Wu, X. Cao, A. Li, D. Yang, X. Lu, G. Wang, X. Han, C. Uher and X. Zhou, *Mater. Today*, 2018, **21**, 501-507.
40. S. Sassi, C. Candolfi, J. B. Vaney, V. Ohorodniichuk, P. Masschelein, A. Dauscher and B. Lenoir, *Appl. Phys. Lett.*, 2014, **104**, 212105.
41. E. K. Chere, Q. Zhang, K. Dahal, F. Cao, J. Mao and Z. Ren, *J. Mater. Chem. A*, 2016, **4**, 1848-1854.

42. Z. H. Ge, D. Song, X. Chong, F. Zheng, L. Jin, X. Qian, L. Zheng, R. E. Dunin-Borkowski, P. Qin, J. Feng and L. D. Zhao, *J. Am. Chem. Soc.*, 2017, **139**, 9714-9720.
43. T. R. Wei, G. Tan, X. Zhang, C. F. Wu, J. F. Li, V. P. Dravid, G. J. Snyder and M. G. Kanatzidis, *J. Am. Chem. Soc.*, 2016, **138**, 8875-8882.
44. K. Peng, X. Lu, H. Zhan, S. Hui, X. Tang, G. Wang, J. Dai, C. Uher, G. Wang and X. Zhou, *Energy Environ. Sci.*, 2016, **9**, 454-460.
45. L. Zhang, J. Wang, Q. Sun, P. Qin, Z. Cheng, Z. Ge, Z. Li and S. Dou, *Adv. Energy Mater.*, 2017, **7**, 1700573.
46. X. Shi, K. Zheng, M. Hong, W. Liu, R. Moshwan, Y. Wang, X. Qu, Z.-G. Chen and J. Zou, *Chem. Sci.*, 2018, **9**, 7376-7389.
47. Y.-M. Han, J. Zhao, M. Zhou, X.-X. Jiang, H.-Q. Leng and L.-F. Li, *J. Mater. Chem. A*, 2015, **3**, 4555-4559.
48. C.-C. Lin, R. Lydia, J. H. Yun, H. S. Lee and J. S. Rhyee, *Chem. Mater.*, 2017, **29**, 5344-5352.
49. C. Han, Z. Li, G. Q. Lu and S. Xue Dou, *Nano Energy*, 2015, **15**, 193-204.
50. X. Liu, Y. Li, B. Zhou, X. Wang, A. N. Cartwright and M. T. Swihart, *Chem. Mater.*, 2014, **26**, 3515-3521.
51. M. Ibanez, R. J. Korkosz, Z. Luo, P. Riba, D. Cadavid, S. Ortega, A. Cabot and M. G. Kanatzidis, *J. Am. Chem. Soc.*, 2015, **137**, 4046-4049.
52. G. Han, S. R. Popuri, H. F. Greer, J. W. Bos, W. Zhou, A. R. Knox, A. Montecucco, J. Siviter, E. A. Man, M. Macauley, D. J. Paul, W. G. Li, M. C. Paul, M. Gao, T. Sweet, R. Freer, F. Azough, H. Baig, N. Sellami, T. K. Mallick and D. H. Gregory, *Angew. Chem. Int. Ed.*, 2016, **55**, 6433-6437.
53. G. Han, R. Zhang, S. R. Popuri, H. F. Greer, M. J. Reece, J. G. Bos, W. Zhou, A. R. Knox and D. H. Gregory, *Materials*, 2017, **10**, 233.
54. W. Liu, K. C. Lukas, K. McEnaney, S. Lee, Q. Zhang, C. P. Opeil, G. Chen and Z. Ren, *Energy Environ. Sci.*, 2013, **6**, 552-560.
55. K. Zhao, C. Zhu, P. Qiu, A. B. Blichfeld, E. Eikeland, D. Ren, B. B. Iversen, F. Xu, X. Shi and L. Chen, *Nano Energy*, 2017, **42**, 43-50.
56. S. A. Yamini, D. R. G. Mitchell, Z. M. Gibbs, R. Santos, V. Patterson, S. Li, Y. Z. Pei, S. X. Dou and G. Jeffrey Snyder, *Adv. Energy Mater.*, 2015, **5**, 1501047.
57. R. J. Korkosz, T. C. Chasapis, S. H. Lo, J. W. Doak, Y. J. Kim, C. I. Wu, E. Hatzikraniotis, T. P. Hogan, D. N. Seidman, C. Wolverton, V. P. Dravid and M. G. Kanatzidis, *J. Am. Chem. Soc.*, 2014, **136**, 3225-3237.
58. G. Han, S. R. Popuri, H. F. Greer, R. Zhang, L. Ferre-Llin, J. G. Bos, W. Zhou, M. J. Reece, D. J. Paul, A. R. Knox and D. H. Gregory, *Chem. Sci.*, 2018, **9**, 3828-3836.
59. M. Hong, Z.-G. Chen, L. Yang, T. C. Chasapis, S. D. Kang, Y. Zou, G. J. Auchterlonie, M. G. Kanatzidis, G. J. Snyder and J. Zou, *J. Mater. Chem. A*, 2017, **5**, 10713-10721.
60. A. C. Larson and R. B. Von Dreele, General Structure Analysis System (GSAS); Los Alamos National Laboratory Report LAUR 86-748; Los Alamos National Laboratory, 1994.
61. B. H. Toby, *J. Appl. Crystallogr.*, 2001, **34**, 210-213.
62. F. K. Lotgering, *J. Inorg. Nucl. Chem.*, 1959, **9**, 113-123.
63. G. D. Moon, S. Ko, Y. Min, J. Zeng, Y. Xia and U. Jeong, *Nano Today*, 2011, **6**, 186-203.
64. A. Banik and K. Biswas, *J. Mater. Chem. A*, 2014, **2**, 9620.
65. X. Wang, J. T. Xu, G. Q. Liu, X. J. Tan, D. B. Li, H. Z. Shao, T. Y. Tan and J. Jiang, *NPG Asia Mater.*, 2017, **9**, e426.
66. J. H. Zhang, J. T. Xu, X. J. Tan, H. X. Wang, G. Q. Liu, H. Z. Shao, B. Yu, S. Yue and J. Jiang, *J. Mater. Chem. C*, 2019, **7**, 2653-2658.
67. S. J. Liang, J. T. Xu, J. G. Noudem, H. X. Wang, X. J. Tan, G. Q. Liu, H. Z. Shao, B. Yu, S. Yue and J. Jiang, *J. Mater. Chem. A*, 2018, **6**, 23730-23735.
68. J. Gao and G. Xu, *Intermetallics*, 2017, **89**, 40-45.
69. T. R. Wei, C. F. Wu, X. Zhang, Q. Tan, L. Sun, Y. Pan and J. F. Li, *Phys. Chem. Chem. Phys.*, 2015, **17**, 30102-30109.
70. B. R. Ortiz, H. Peng, A. Lopez, P. A. Parilla, S. Lany and E. S. Toberer, *Phys. Chem. Chem. Phys.*, 2015, **17**, 19410-19423.

View Article Online
DOI: 10.1039/C9TC01994D

Table of Contents

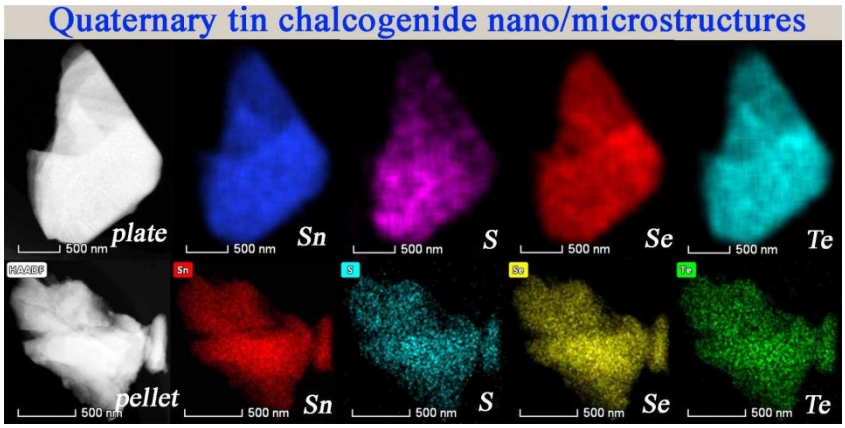

Nanostructured $SnS_{0.1}Se_{0.9-x}Te_x$ quaternary chalcogenides have been synthesized via anion exchange; sintered $SnS_{0.1}Se_{0.88}Te_{0.02}$ achieves enhanced electrical properties in the low-temperature range.